Refinement of Analytical Current Waveform for Acoustic Noise Reduction in Switched Reluctance Motor

FARES S. EL-FAOURI ⓘ **(Graduate Student Member, IEEE), YIFEI CAI** ⓘ **(Graduate Student Member, IEEE), AND AKIRA CHIBA** ⓘ **(Fellow, IEEE)**

Department of Electrical and Electronic Engineering, Tokyo Institute of Technology, Tokyo 152-8550, Japan

CORRESPONDING AUTHOR: FARES S. EL-FAOURI (email: el.f.ab@m.titech.ac.jp)

ABSTRACT In this article, a refinement algorithm of the current waveform that flattens the radial-force sum in switched reluctance motors is proposed. Flattening the radial-force sum eliminates the multiples of the third radial-force component. These components excite the breathing mode vibration, which is typically the dominant vibration in switched reluctance motors with a high number of poles. The previously proposed analytical current derivation for flattening the radial-force sum neglects magnetic saturation, limiting its applicability to low-torque region. Consequently, for high-torque saturation conditions, the previous waveform shaping degrades in flattening the radial-force sum. The proposed refinement of the analytical current waveform addresses this limitation, enabling effective radial-force sum flattening even under high-torque conditions. Additionally, the proposed current exhibits significantly lower peaks than those of the flattening methods at high-torque region in the literature, mitigating the need for higher-rated inverters. Finite element analysis and experimental validation verify the effectiveness of the proposed method.

INDEX TERMS Acoustic noise reduction, mode 0 vibration, radial force sum flattening, switched reluctance motor (SRM).

I. INTRODUCTION

Advances in motor-drive methods have propelled the adoption of switched reluctance motors (SRMs). Renowned with high torque density, efficiency, and robustness, SRMs offer the additional advantage of being free from rare-earth materials, leading to significant cost reductions. Nevertheless, the inherent doubly-salient structure and conventional current excitation in SRMs give rise to considerable harmonics in radial force. These harmonics induce significant stator vibration and acoustic noise.

The literature has extensively addressed the reduction of acoustic noise in SRMs from various perspectives. Regarding the SRM structure, it was reported in [1] that installing stator-pole bridges resulted in reduction of vibration and acoustic noise. In terms of rotor structures, curving the rotor poles in the stack direction led to reductions in both radial force variation and torque ripple [2]. Proposing a triangular shape in the middle of the rotor structure is reported to reduce radial-force

variation [3]. Other research endeavors addressed the radial force and torque ripple issues by optimizing rotor flux barriers [4], proposing a cylindrical rotor structure [5], introducing leaf springs onto the stator back yoke [6], engraving windows into the stator and rotor poles [7], and skewing the stator and rotor [8].

From the motor drive and inverter operation perspective, it is reported that SRM vibration and acoustic noise can be reduced by two-stage commutation [9], hybrid excitation using C-dump inverter [10], active vibration cancellation [11], and smoothening the voltage commutation during the turn-OFF stage [12]. Furthermore, Guo et al. [13] provided an analytical derivation for determining the optimal turn-ON angle to mitigate resonance vibrations.

Radial-force waveform shaping was the subject of several researches in the literature aiming to reduce the vibration and acoustic noise of SRMs. In [14], a Gaussian reference was proposed for radial-force shaping, with parameters tailored to

mitigate dominant vibration modes. The study primarily focused on eliminating the vibration modes in a low stator-pole number SRM. Another research proposed using the logistic function for shaping the radial force in a high stator-pole number SRM [15]. However, the method in that research exhibited a considerable current peak post the unaligned position.

Current waveform shaping for SRM acoustic noise reduction was approached from numerous studies in the literature. Radial-force sum flattening, being one of the current-waveform shaping methods, was first introduced in [16]. This method involves shaping the current waveform offline through a mathematical derivation of the current reference. In that study, the current was defined to have up to the third harmonic component, assuming zero phase shifts for simplicity. Subsequent work in [17], [18], and [19] incorporated the phase shifts numerically rather than mathematically, resulting in minimal torque ripple and rms current waveforms. However, heavy numerical sweep was required for the determination of the current parameters. The complete analytical derivation of the current waveform that flattens the radial-force sum, including the current phase shifts, was introduced in [20]. Nonetheless, magnetic saturation was not considered in that derivation. Consequently, the effectiveness of that method in flattening the radial-force sum at the high-torque region was limited.

Another aspect of research focused on radial-force sum flattening by control strategies. The triangle-width strategy [21], direct instantaneous force control [22], and differential evolution optimization [23] were reported to contribute to flattening the radial force and reducing the acoustic noise. Investigation of simultaneous torque and radial-force ripple reduction was conducted in [24] by numerical sweeping. The radial-force sum flattening technique has been noted for its effectiveness in SRMs characterized by a high stator-pole number, notably traction SRMs [25].

This article introduces a refinement algorithm for the analytical derivation method outlined in [20], aimed at extending its effectiveness to the high-torque saturation region. The proposed refinement has two main advantages. First, it does not involve numerical sweeping of parameters. Second, the proposed current waveform exhibits a significantly lower peak than that in [15], despite the same effectiveness of both methods in flattening the radial-force sum at high-torque conditions. This reduction in peak current values translates to potential cost savings by alleviating the need for a larger inverter.

The rest of this article is organized as follows. Section II explains the proposed method, Section III presents the FEA results, Section IV shows the experimental results, and Section V concludes this article.

II. PROPOSED METHOD
A. SRM RADIAL FORCE AND VIBRATION MODES
Normal operation of SRMs involves the concurrent variation of radial force in both time and space. The spatial components dictate the shape of the radial-force distribution [14], [26]. For instance, the spatial order 0 implies that the radial-force distribution is spatially forming the circular breathing mode. A spatial order 2 signifies an oval-shaped radial-force distribution, and so forth.

Identifying the dominant spatial vibration modes is followed by identifying the temporal radial-force components responsible for exciting them. Typically, the number of phases, stator poles, and rotor poles identify the dominant spatial vibration modes and their corresponding temporal components [26]. In a three-phase 18/12 SRM, the breathing vibration mode with spatial order 0 is dominant and is excited by the multiples of the third temporal radial-force component. Conversely, in a three-phase 6/10 SRM, the breathing mode is not problematic; instead, mode 2 poses the issue.

It was shown in [16] that radial-force sum flattening eliminates the multiples of the third radial-force component. Therefore, radial-force sum flattening effectively eliminates breathing mode vibration in 18/12 SRMs, leading to notable reductions in acoustic noise. The adopted SRM configuration in this study is the 18/12 SRM. There are two reasons for adopting that configuration: First, it was confirmed in [27] that the 18/12 configuration exhibits the highest torque density. Second, the radial-force sum flattening is effective on SRMs with a high number of stator poles [25]. The effectiveness of radial-force sum flattening on a 36/24 and 18/12 SRMs was previously verified in [16] and [18], respectively. However, at low stator-pole number, such as a 6/10 SRM, radial-force sum flattening was not effective [28]. Since the proposed method in this article aims to refine the previous radial-force sum flattening method in [20], the 18/12 SRM configuration was adopted in this study.

It is worth noting that the radial force is the primary contributor to vibration and acoustic noise in SRMs [29]. Specifically, the frequency and variation of the radial force are the key features that generate acoustic noise. When the radial force frequency matches any of the motor's natural frequencies, significant acoustic noise can occur. Additionally, greater variation in radial force leads to increased acoustic noise. In SRMs with a high number of stator poles, the focus is on the variation of the sum of the radial forces [16], which is characterized by the third harmonic component of the radial force and its multiples.
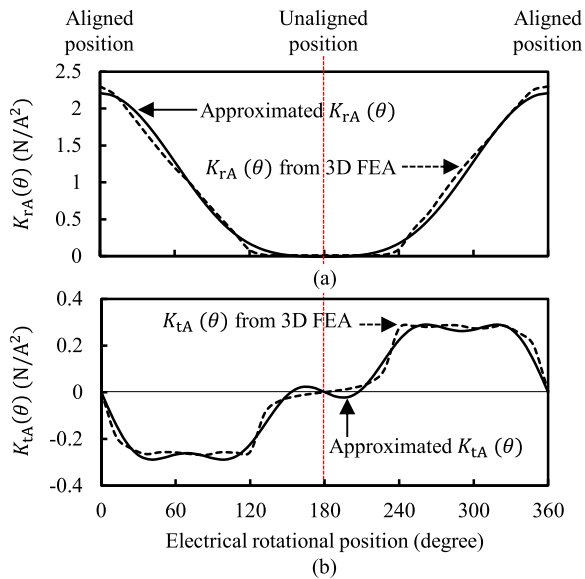
B. RADIAL AND TANGENTIAL FORCE CHARACTERISTICS
Let us define the rotor position θ to be $0°$ at the A-phase aligned position. The mathematical expressions for the temporal radial and tangential forces of A-phase are given in [30] as follows:

$$F_{\mathrm{rA}}(\theta) = K_{\mathrm{rA}}(\theta)\, i_{\mathrm{A}}(\theta)^2 \tag{1}$$

$$F_{\mathrm{tA}}(\theta) = K_{\mathrm{tA}}(\theta)\, i_{\mathrm{A}}(\theta)^2 \tag{2}$$

where $i(\theta)$ represents the instantaneous current value, and $K_{\mathrm{r}}(\theta)$, $K_{\mathrm{t}}(\theta)$ denote the radial and tangential force factors, respectively. These factors depend on the SRM specifications,

FIGURE 1. SRM radial and tangential force characteristics for A-phase at a specific current value. (a) Radial force characteristics. (b) Tangential force characteristics.
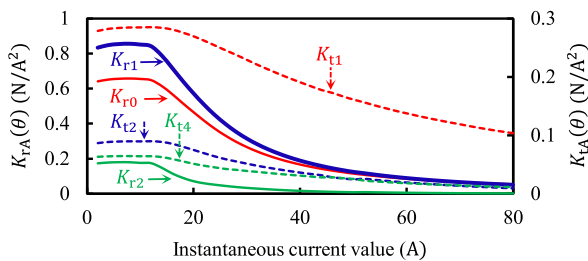
FIGURE 2. Current-dependence of major frequency components of radial (solid) and tangential (dashed) forces.

and are determined through FEA. Fig. 1 shows $K_r(\theta)$ and $K_t(\theta)$ under a specific current excitation. These factors can be analytically approximated by their Fourier-series expansions, expressed as follows:

$$K_{rA}(\theta) = K_{r0} + K_{r1}\cos(\theta) + K_{r2}\cos(2\theta) \quad (3)$$

$$K_{tA}(\theta) = -K_{t1}\sin(\theta) - K_{t2}\sin(2\theta) - K_{t4}\sin(4\theta). \quad (4)$$

The analytically approximated curves, depicted in Fig. 1, demonstrate a close correspondence with the FEA curves. Notably, the six coefficients K_{r0}, K_{r1}, K_{r2}, K_{t1}, K_{t2}, and K_{t4} in (3) and (4) remain constants in the magnetically-linear region, but they transition to functions of the current in the magnetically-saturated region. Appendix I lists these coefficients in the linear region for the SRM under study. Fig. 2 shows the diminishing values of $K_r(\theta)$ and $K_t(\theta)$ coefficients as the current increases. The solid curves represent the radial-force coefficients K_{r0}, K_{r1}, and K_{r2}, while the dashed curves represent the torque coefficients K_{t1}, K_{t2}, and K_{t4}. It is essential to note that the mathematical current derivation in [20] assumed constant values for these six coefficients. As depicted in Fig. 2, this

approach resulted in inaccuracies in the high-torque region, as the reductions in the coefficients with increasing current were not accounted for. This led to compromising the effectiveness of flattening the radial-force sum at high torque.

C. LIMITATIONS OF THE ANALYTICAL CURRENT DERIVATION AT THE HIGH-TORQUE REGION

The complete analytical derivation of the current waveform, including phase shifts, is introduced in [20] for flattening the radial-force sum. In [20], the current waveform is provided as follows:

$$\begin{aligned} i_A(\theta)^{\text{original}} &= I_0 + I_1\sin(\theta + \phi_1) \\ &\quad + I_2\sin(2\theta + \phi_2) + I_3\sin(3\theta + \phi_3) \quad (5) \end{aligned}$$

where I_0, I_1, I_2, I_3, ϕ_1, ϕ_2, and ϕ_3 are the seven current parameters, and are determined from the offline mathematical equations detailed in [20]. These parameters are determined based on two purposes: achieving the target average torque, and flattening the radial-force sum. For instance, I_0 is obtained in [20] by

$$I_0 = \frac{2\left(-\frac{\sqrt{3}}{8}I_1^2 K_{t2} + \frac{T_{av}^{\text{math}}}{3R}\right)}{\sqrt{3}I_1\left(K_{t1} - \frac{K_{r1}K_{t2}}{4K_{r0}}\right)} \quad (6)$$

where R is the rotor radius, and T_{av}^{math} is the target average torque value inputted into the mathematical equations. Similar to (6), the remaining six current parameters are calculated in [20] from K_r and K_t coefficients. However, these coefficients are assumed to be constants in [20], which is only applicable in the low-torque region, as indicated in Fig. 2. Consequently, the effectiveness of the method in [20] is limited in the high-torque saturation region. This article aims to extend the applicability of the analytically-derived current to the high-torque saturation region by proposing a refinement algorithm of $i_A(\theta)^{\text{original}}$ in (5). The mathematical expression for the third component of the radial-force sum, which is the largest component, has been derived in [20] and is presented in Appendix II of this article.

First, it is essential to identify the limitations of the analytical derivation method outlined in [20] within the high-torque region. To achieve this, the SRM under investigation is subjected to two FEA cases using the analytical derivation method: one within the magnetically-linear region and another within the heavily saturated region.

Fig. 3(a) illustrates the two A-phase currents derived using the analytical method outlined in [20] with a low T_{av}^{math} value for the linear case, and a high T_{av}^{math} for the saturated case. For the linear case, the derived current waveform can generate an FEA average torque value T_{av}^{FEA} close to the target average torque value T_{av}^{math} because the K_t coefficients are precisely modeled in the linear case in [20]. On the other hand, since the decrease of K_t coefficients in the saturation region is not modeled, the method in [20] lost its accuracy in torque prediction. Notably, Fig. 3(b) compares the waveforms of the ratio T/T_{av}^{math}. It is apparent that in the linear region, the calculated average torque value T_{av}^{math} closely matched the FEA average
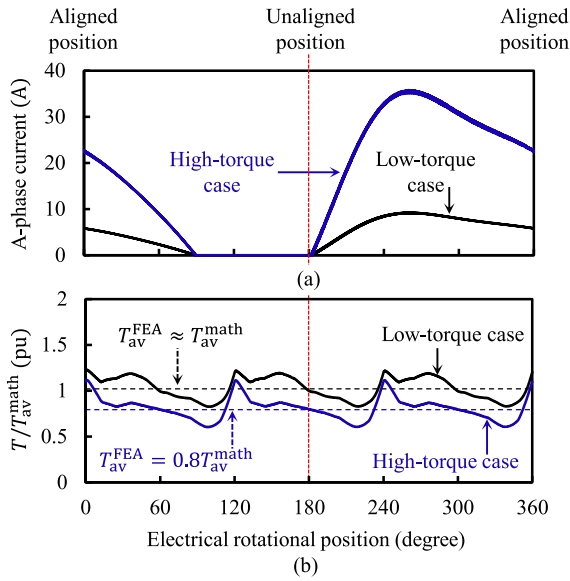
FIGURE 3. Comparison of the analytical derivation method in [20] at low and high-torque cases. (a) Current waveforms. (b) Torque waveforms normalized by T_{av}^{math}.
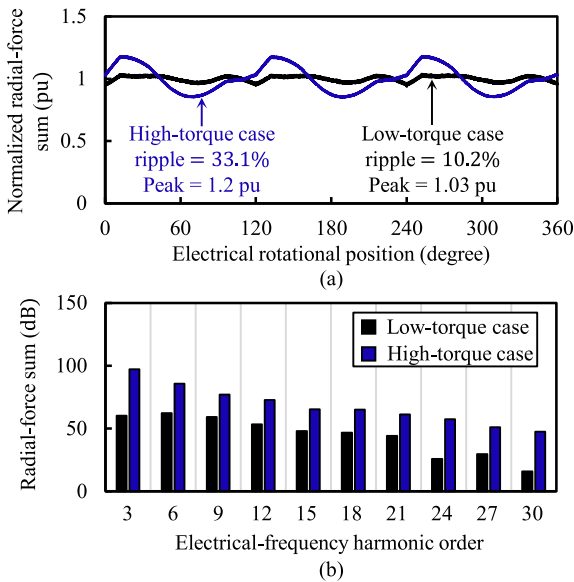
FIGURE 4. Comparison of the analytical derivation method in [20] at low and high-torque cases. (a) Normalized radial-force sum waveforms. (b) Frequency spectra of the radial-force sum.

torque T_{av}^{FEA}, whereas in the saturated region, T_{av}^{FEA} is 20% lower.

Fig. 4 demonstrates the normalized radial-force sum waveforms and spectra. It is evident that the performance of flattening degraded significantly under the heavily-saturated condition, since the decrease of K_r coefficients in the saturation region is not modeled in [20]. This degradation is notably reflected in the increased presence of the multiples of the third component.
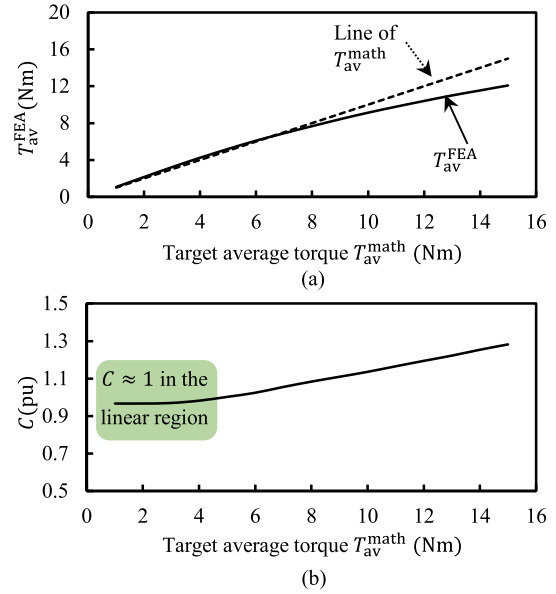
FIGURE 5. (a) Relationship between the average torque value in the mathematical model in [20] T_{av}^{math} and the obtained average torque T_{av}^{FEA} for the SRM under study. (b) Compensation factor required for matching T_{av}^{math} with T_{av}^{FEA}.

In conclusion, the saturation condition affects the analytical method described in [20] in two significant ways.
1) Achieving the required torque.
2) Effectiveness of flattening the radial-force sum.

D. REFINEMENT OF THE ANALYTICAL CURRENT DERIVATION METHOD

The proposed refinement is divided into two stages. The first stage aims to enhance the analytical derivation method to achieve the necessary average torque even in magnetically-saturated conditions. Subsequently, the second stage of refinement focuses on flattening the radial-force sum, particularly within these magnetically-saturated conditions.

For the first stage, which involves attaining the necessary average torque value, a saturation-compensation factor C is introduced to raise the target mathematical average torque value T_{av}^{math} in [20] to account for the torque degradation, as follows:
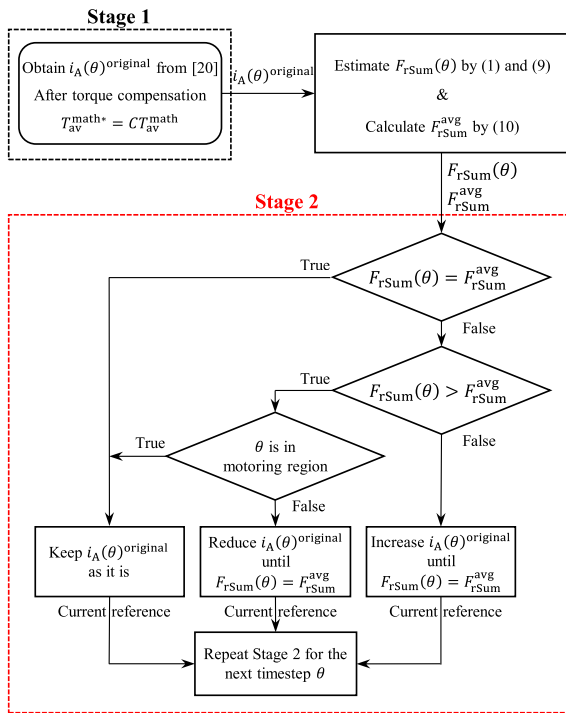
$$C = \frac{T_{av}^{math}}{T_{av}^{FEA}}. \qquad (7)$$

Then, the new compensated target average torque T_{av}^{math*} is set as follows:

$$T_{av}^{math*} = CT_{av}^{math}. \qquad (8)$$

Fig. 5(a) illustrates the relationship between T_{av}^{math} and T_{av}^{FEA} in the studied SRM. It can be observed that T_{av}^{FEA} falls lower than T_{av}^{math} in the high-torque region. The compensation factor C calculated from (7) is shown in Fig. 5(b). As shown in Fig. 5(b), C is nearly 1 in the linear region where the K_t coefficients are well modeled, and the torque is precisely predicted. On the other hand, C is larger than 1 and increases as
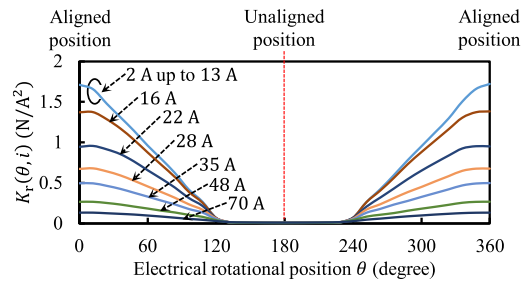
FIGURE 6. Proposed refinement algorithm for A-phase. The first refinement stage incorporates the compensation of the average torque. The second refinement stage involves flattening the radial-force sum.

FIGURE 7. Radial force characteristics of the SRM under study at various current values.

sum can then be obtained as follows:

$$F_{\text{rSum}}(\theta) = F_{\text{rA}}(\theta) + F_{\text{rB}}(\theta) + F_{\text{rC}}(\theta). \tag{9}$$

Upon completion of one steady-state electrical period 2π, the average of (9) is calculated as follows:

$$F_{\text{rSum}}^{\text{avg}} = \frac{1}{2\pi} \int_0^{2\pi} F_{\text{rSum}}(\theta) \, d\theta. \tag{10}$$

Equation (10) represents the dc component of the $F_{\text{rSum}}(\theta)$ waveform. The importance of obtaining the $F_{\text{rSum}}^{\text{avg}}$ value lies in its correlation to the desired average torque value. Under the excitation $i_A(\theta)^{\text{original}}$ of the method in [20], each average torque value corresponds to a unique $F_{\text{rSum}}^{\text{avg}}$ value. It should be emphasized that the previous sentence only holds true under the same excitation of $i_A(\theta)^{\text{original}}$; any two different current waveforms with the same average torque are most likely not sharing the same average radial-force sum. Therefore, $F_{\text{rSum}}^{\text{avg}}$ is set as the target flat value for the radial-force sum at the target average torque achieved by $i_A(\theta)^{\text{original}}$.

In *Stage 2* of Fig. 6, the estimated radial-force sum $F_{\text{rSum}}(\theta)$ is compared with $F_{\text{rSum}}^{\text{avg}}$ at each timestep. Based on the comparison result, the excitation current is modified to finally make $F_{\text{rSum}}(\theta) = F_{\text{rSum}}^{\text{avg}}$ at every timestep. If $F_{\text{rSum}}(\theta) = F_{\text{rSum}}^{\text{avg}}$, no change of $i_A(\theta)^{\text{original}}$ is required at that timestep, as shown by the left-bottom block of *Stage 2* in Fig. 6. However, if $F_{\text{rSum}}(\theta)$ falls below $F_{\text{rSum}}^{\text{avg}}$, the original current value $i_A(\theta)^{\text{original}}$ will be increased at that timestep until $F_{\text{rSum}}(\theta)$ value increases sufficiently to be equal to $F_{\text{rSum}}^{\text{avg}}$, as shown by the right-bottom block of Fig. 6. Conversely, if $F_{\text{rSum}}(\theta)$ exceeds $F_{\text{rSum}}^{\text{avg}}$, $i_A(\theta)^{\text{original}}$ value at that timestep has to be decreased. However, it is crucial to avoid reducing $i_A(\theta)^{\text{original}}$ in the motoring region represented by the positive $K_{\text{tA}}(\theta)$ region in Fig. 1(b). The positive region of $K_{\text{tA}}(\theta)$ spans from $180°$ up to $360°$, as visible in Fig. 1(b). Decreasing the current in the motoring region can adversely affect achieving the target average torque, thus compromising the first stage of refinement. Therefore, decreasing $i_A(\theta)^{\text{original}}$ is only permissible outside of the motoring region. An exception is made for the last portion of the motoring region, coinciding with the commutation zone from $336°$ to $360°$, where it is unavoidably necessary to adjust $i_A(\theta)^{\text{original}}$ to achieve the radial-force sum flattening. Decreasing the current in this commutation

the torque value increases in the saturation region, indicating the increasing torque degradation. The first stage of refinement involves compensating the average torque degradation by increasing the target average torque value $T_{\text{av}}^{\text{math}}$ by the factor C based on (8).

Fig. 6 depicts the refinement algorithm for the A-phase current. The currents of A, B, and C-phases undergo identical refinements, each separated by $120°$ phase shifts. The starting point of the refinement is *Stage 1*; obtaining the analytically-derived current waveform $i_A(\theta)^{\text{original}}$ in (5) after the torque compensation. The obtained current $i_A(\theta)^{\text{original}}$ will then be used to estimate the radial-force sum waveform $F_{\text{rSum}}(\theta)$, as shown in the upper-right part of Fig. 6. The estimation of radial force waveform is essential for the second stage of refinement. While it is possible to measure radial force using strain gauges, as demonstrated in [31], this article opts to estimate radial force using an offline two-dimensional lookup table of $K_r(\theta, i)$. The radial-force characteristics $K_r(\theta, i)$ is computed through FEA prior to applying the proposed refinement. In this study, virtual work principle is adopted in the computation of the radial-force characteristics, which are then used as a lookup table for the estimation process. Fig. 7 demonstrates $K_r(\theta, i)$ lookup table at several example current values. Note that $K_r(\theta, i)$ remains unchanged in the magnetically-linear region (2 A up to 13 A) owing to the constant magnetic permeability in that region. Subsequently, radial force can be estimated at each rotor position θ and each current value i by applying (1). The estimated radial-force

zone is allowed for two reasons: First, the impact of current modification on torque is small because $K_{tA}(\theta)$ is low in this commutation zone, as shown in Fig. 1(b). Second, $K_{rA}(\theta)$ is the highest in the same commutation zone, as shown in Figs. 7 and 1(a), indicating that a slight change in current can significantly improve the shape of radial-force sum. The extent of the commutation zone can be adequately set as 20% of the $120°$ overall conduction zone for each phase. This translates to $24°$ of commutation. To summarize, the reduction of $i_A(\theta)^{original}$ is only permitted in two regions: the generating region where $K_{tA}(\theta)$ is negative ($0° < \theta < 180°$) and the commutation zone ($336° < \theta < 360°$). Outside of these two regions, the reduction of $i_A(\theta)^{original}$ is not permissible, even if $F_{rSum}(\theta)$ exceeded F_{rSum}^{avg}. In such an occasion, $i_A(\theta)^{original}$ will be kept the same without any change.

It is worth noting that the adjustment of $i_A(\theta)^{original}$ can be achieved by fixed increments or decrements, provided the sampling frequency of the model-based software remains very high and ideal inverter switches are used. In this scenario, the exact value of the increment or decrement is not critical as long as it suffices to reach the desired current value. This is because the fast sampling allows the controller to instantaneously readjust the reference command, while the actual current changes more slowly and smoothly due to the coil inductance.

The refined current waveform is then obtained as $i_A(\theta)^{refined}$, and it serves as the reference current for the hysteresis current controller in the experiment. This controller is responsible for driving the SRM inverter by regulating the measured current $i_A(\theta)$ to track the refined reference $i_A(\theta)^{refined}$.

III. FEA RESULTS

A. REFINEMENT OF THE ANALYTICAL DERIVATION METHOD

The SRM under study is a three-phase 18/12 SRM designed as a generator for hybrid vehicle applications. The SRM was initially designed in [32] to be competitive with the fourth-generation of Toyota Prius' permanent-magnet generator. The initial design included an effective water-cooling system. Table 1 presents the SRM specifications. Note that the iron-core material is high-silicon 10JNEX900 steel, which exhibits negligible magnetostriction characteristics [33], [34]. The selection of 10JNEX900 ensures that radial force is the sole contributor to vibration and acoustic noise.

Fig. 8 shows the FEA results of the current, radial-force sum, and torque waveforms at 12 Nm before and after refinement. Two cycles are shown in Fig. 8: the first cycle spans from $0°$ to $360°$, during which the unrefined $i_A(\theta)^{original}$ from [20] is applied. The waveforms obtained under the refined current are shown in the second cycle from $360°$ to $720°$. Evidently, the refined current effectively flattens the radial-force sum, while at the same time, the average torque, torque ripple, and rms current were not impacted by the refinement process. This underscores the effectiveness of the refinement method

TABLE 1. SRM Specifications

| Specification	Unit	Original design value	Experimental limitation
Stator poles	-	18	-
Rotor poles	-	12	-
Stator outer diameter	mm	190	-
Rotor outer diameter	mm	133	-
Air gap at the aligned position	mm	0.3	-
Stack length	mm	52	-
dc bus voltage	V	600	400
Maximum speed	r/min	20000 (single-pulse drive)	1900
Maximum torque	Nm	15 ~ 20 (water cooling) 8 (no cooling)	6.8
Maximum power	kW	42 (water cooling)	1.5
Maximum rms current	A	25 (water cooling)	15
Number of turns per tooth	-	110	-
Number of parallel paths per tooth	-	5	-
Core material	-	10JNEX900 steel	-
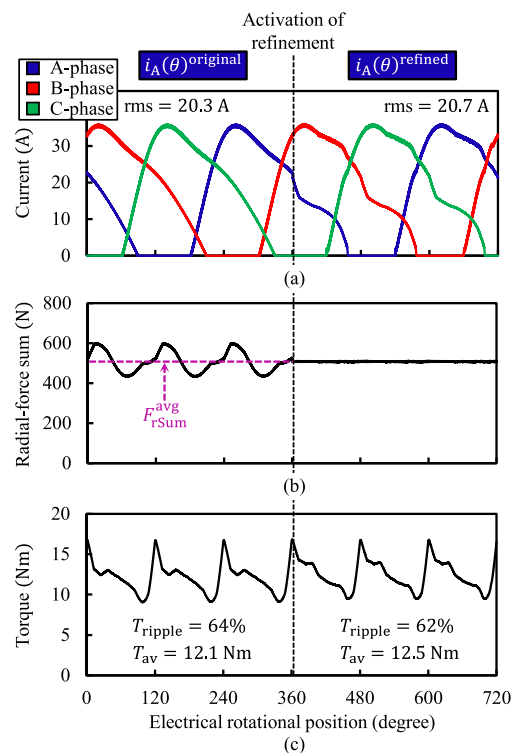
FIGURE 8. FEA comparison between the analytically-derived current from [20] and the proposed refined current in terms of (a) current waveforms, (b) radial-force sums, and (c) torque waveforms.

in flattening the radial-force sum without compromising the other crucial performance metrics.

Fig. 9 shows how the operation of refinement in Fig. 8 took place in detail. The estimated radial-force sum $F_{rSum}(\theta)$ resulting from applying the unrefined currents $i_{A,B,C}(\theta)^{original}$ exhibit six peaks, as shown in Fig. 9. Three peaks are above F_{rSum}^{avg}, while the other three are below it. For example, the first peak of $F_{rSum}(\theta)$ occurs after $\theta = 0°$ up until $\theta = 50°$. The
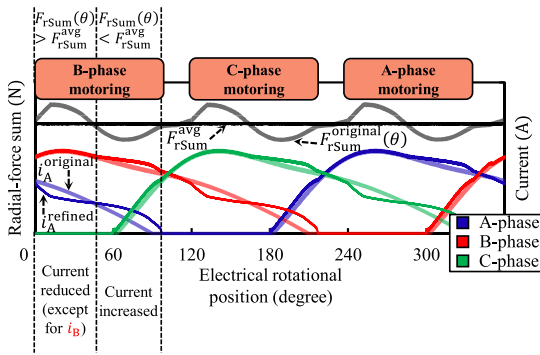
FIGURE 9. Algorithm response to the radial-force sum peaks that exceed or fall below F_{rSum}^{avg}. As an example, the response to the first two peaks is shown.

first peak is exceeding F_{rSum}^{avg}. At that particular duration of the first peak, two currents are being provided, namely i_A and i_B, while i_C is zero. The refinement algorithm dictates reduction of the current in this situation since $F_{rSum}(\theta) > F_{rSum}^{avg}$. However, i_B will not be reduced to prevent loss of torque since that specific region ($0° < \theta < 50°$) lies in the B-phase motoring region. Hence, i_A will be solely reduced. On the other hand, from $\theta = 50°$ up to $\theta = 100°$, $F_{rSum}(\theta)$ is less than F_{rSum}^{avg}. Consequently, the current is increased until $F_{rSum}(\theta) = F_{rSum}^{avg}$. It is noteworthy that the aforementioned current increase does not occur at the same ratio for all three phases, due to the varying $K_r(\theta, i)$ values for each phase at a given position.

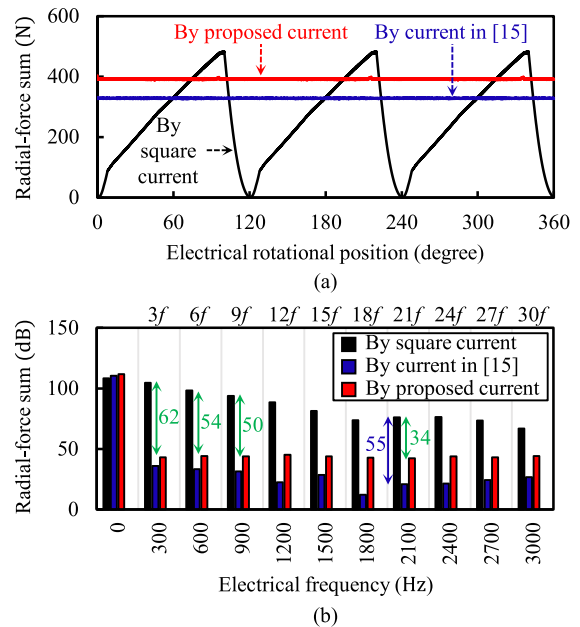### B. PROPOSED METHOD COMPARISON WITH CONVENTIONAL SQUARE AND RADIAL-FORCE SHAPING METHODS

The proposed method is compared against the conventional square current and the previously proposed radial-force shaping method in [15]. This comparison is particularly significant because the method outlined in [15] was specifically devised to address the limitation of the analytical derivation method presented in [20], namely the inability to achieve radial-force sum flattening at high-torque conditions. However, the method in [15] has a drawback of requiring a significantly high peak current value to flatten the radial force sum. Thus, the comparison with [15] aims to demonstrate the superiority of the proposed method in this study in reducing the peak current observed in [15], while successfully flattening the radial-force sum in the high-torque region. The comparison point is designated at 7.4 Nm and 500 r/min.

Fig. 10 shows the comparison of the A-phase current waveforms between the conventional square current, the current outlined in [15], and the proposed current. Particularly noteworthy is the 25.3% reduction in the peak current observed with the proposed current compared to that in [15]. This significant reduction of the peak current allows for the use of smaller inverters. Additionally, a 2.6% reduction in rms current is observed compared with the current in [15].

Fig. 11 illustrates the comparison of the radial-force sum, showcasing both waveforms and spectra. Both the method
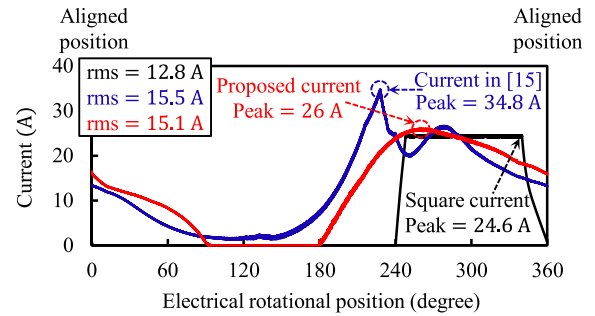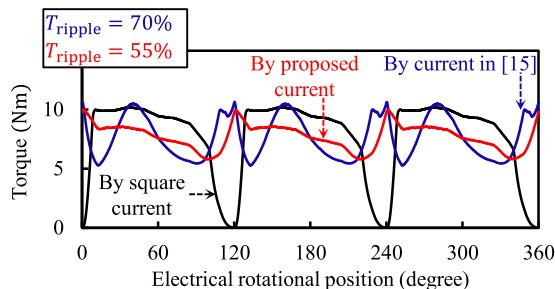

FIGURE 10. FEA comparison of A-phase current waveforms between the conventional square method, radial-force shaping method in [15], and the proposed method.

FIGURE 11. FEA comparison of radial-force sums between the conventional square method, radial-force shaping method in [15], and the proposed method. (a) Waveforms. (b) Frequency spectra.

proposed in [15] and the proposed method effectively flattened the radial-force sum, resulting in a significant reduction in the multiples of the third radial-force component. In Fig. 11(b), it is worth noting that a 30-dB reduction corresponds to a 99.9% reduction. Although the current in [15] reduces the force components more than the proposed current does, the reduction effect is considered the same in practice because reductions of 30 dB (99.9%) and 40 dB (99.99%) are not distinguishable in experimental vibration measurements. For instance, the method in [15] reduced the 21st component by 55 dB (99.9997%), which is more than the reduction of 34 dB (99.96%) achieved by the proposed method. However, these two reduction values will not result in experimental distinction.

Fig. 12 presents a comparison of the torque waveforms. Compared with the method in [15], the proposed method exhibited a 15 percentile-point reduction in torque ripple.

FIGURE 12. FEA comparison of torque waveforms at 7.4 Nm between the conventional square method, radial-force shaping method in [15], and the proposed method.

Moreover, due to the refinement algorithm preventing current reduction in the motoring region, the proposed method maintains the average torque intact.

C. EFFECTIVENESS OF PROPOSED METHOD IN FLATTENING THE RADIAL-FORCE SUM AT MAXIMUM CURRENT OPERATION

The effectiveness of the proposed method becomes more pronounced as the operation delves deeper into the magnetically-saturated region. Therefore, in this subsection, radial-force sum flattening is compared at the maximum operating phase rms current of the SRM, which is 25 A.

Fig. 13(a) illustrates the comparison at 15 Nm, 500 r/min between the unrefined original current $i_A(\theta)^{original}$ and the proposed refined current at the maximum rms current operation of 25 A. As shown in Fig. 13(b), the resultant radial-force sum with the proposed method is flat even at the maximum current operation. The variation of the radial-force sum was reduced by 32 percentile points. Additionally, the FFT frequency spectra in Fig. 13(c) reveal that all multiples of the third radial-force sum component have been effectively decreased, with some reductions reaching up to 39 dB.

IV. EXPERIMENTAL RESULTS

Fig. 14 shows the experimental setup utilized in this study. The SRM is coupled to an interior permanent-magnet synchronous motor (IPMSM) through a torque detector. The rotational speed of the system is controlled by the inverter driving the IPMSM. The detected rotor position and currents are fed into the control system (Myway Plus PE-EXPERT 4) which generates the gate signals for the SRM inverter. The SRM housing contains three windows that reveal the stator core underneath. The windows are spaced 120 mechanical degrees apart, as shown in Fig. 14(b). Accelerometers (Ono Sokki NP-3000) were installed directly on the stator core through the windows for vibration measurement. Specifically, three accelerometers were positioned in the middle of each of the three windows. Additionally, a sound pressure level (SPL) microphone (RION UC-59) was employed to detect SPL variations. The measured signals from both the accelerometers
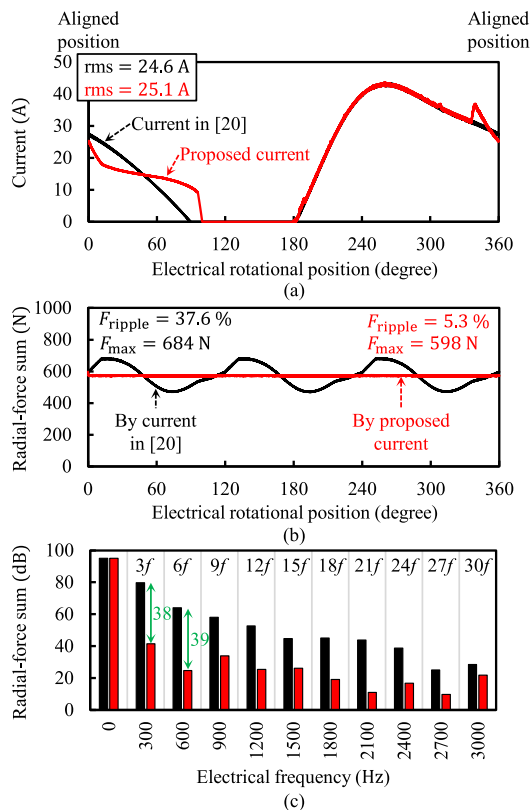
FIGURE 13. FEA comparison of the original unrefined current $i_A(\theta)^{original}$ and the proposed refined current at the maximum rms current operation of 25 A. (a) A-phase current waveforms. (b) Radial-force sums. (c) Frequency spectra of the radial-force sums.
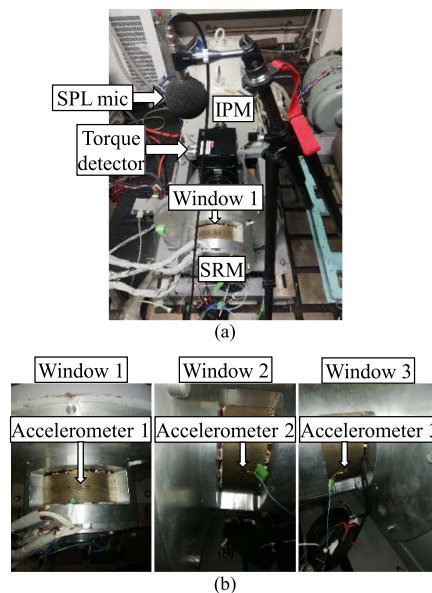
FIGURE 14. Experiment setup. (a) Testbed and microphone. (b) Accelerometers installed on the SRM windows.

TABLE 2. Comparison Between Experimental and FEA Average Torque Values at Various Square-Current Excitations

Square-current reference (A)	Measured average torque in experiment (Nm)	Calculated average torque by FEA (Nm)
8.1	1	1.04
11.5	2	2.05
14.2	3	3.12
16.5	4	4.14
18.7	5	5
20.7	6	5.98
22.5	7	6.81
24.6	8	7.9

and the microphone were directed to the sound and vibration analysis system (O-Solution DS-5000), which provides detailed frequency spectra analyses of acceleration and sound pressure level. The torque and mechanical rotational speed were set at 6.8 Nm and 500 r/min.

The current is controlled by a hysteresis current controller. The built-in current sensors in the SRM inverter are used to measure the current and provide feedback to the controller. A hysteresis band of 0.1 A was used. The measured current is compared with the upper and lower hysteresis bands of the provided reference current. Accordingly, the references of the proposed current, as well as the previously proposed currents in [15] and [20] can be tracked. The switching frequency of the IGBT inverter is 20 kHz.

Applying the proposed current involves ensuring correspondence between the FEA model and the SRM under test. If good correspondence is present, the FEA current can be used as the reference current in the experiment. Otherwise, new lookup tables of the compensation factor C, radial and tangential-force characteristics $K_r(\theta, i)$, $K_t(\theta, i)$ need to be obtained experimentally rather than through FEA. These new tables can then be used to apply the proposed method.

Table 2 demonstrates a torque comparison conducted between the experiment and the FEA to validate their correspondence. The comparison involved eight points of square current excitation, ranging from 1 Nm (average torque) to 8 Nm. The sampling frequency, speed, turn-ON angle, and turn-OFF angle were unified between the experiment and FEA at 20 kHz, 1000 r/min, 230°, and 340° (for A-phase), respectively. The dc bus voltage and the square current reference value at each torque point were also unified between the experiment and FEA. Table 2 lists the obtained comparison results between the FEA model and the test SRM, which exhibit good correspondence at all torque values. Therefore, the FEA-computed compensation factor C and estimated radial force can be applied to the experiment.

A. PROPOSED METHOD COMPARISON WITH CONVENTIONAL SQUARE AND RADIAL-FORCE SHAPING METHODS

Fig. 15 illustrates the comparison of the A-phase currents obtained experimentally. Three currents are compared: the conventional square current, the previously proposed current in [15], and the proposed refined current at 6.8 Nm. Notably,
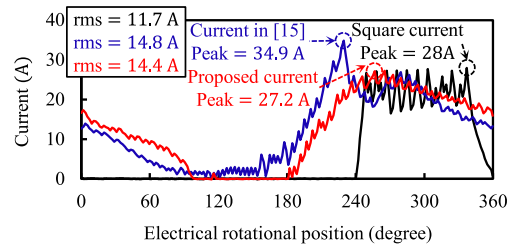
FIGURE 15. Experimental comparison of A-phase current waveforms between the conventional square method, radial-force shaping method in [15], and the proposed method.
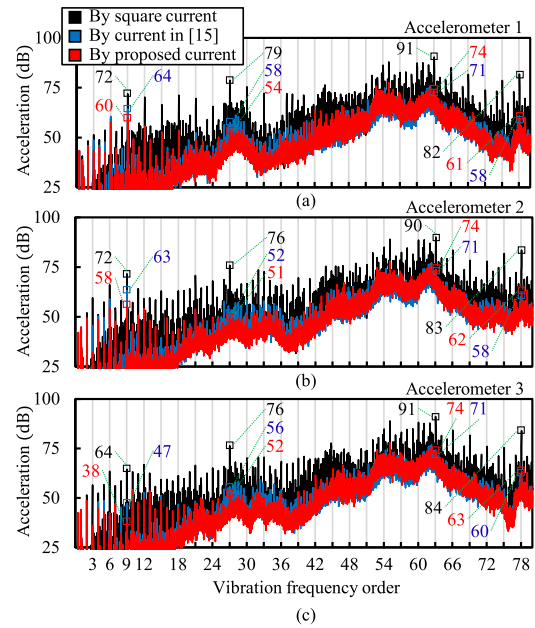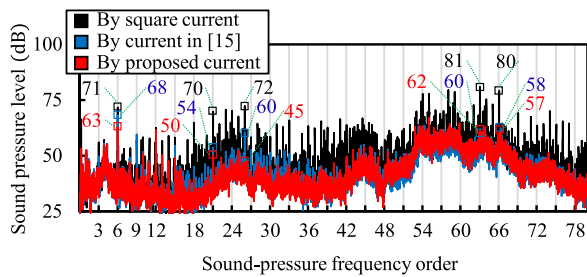

FIGURE 16. Experimental comparison of stator acceleration spectra between the conventional square method, radial-force shaping method in [15], and the proposed method at the centers of windows (a) 1, (b) 2, and (c) 3.

the peak of the proposed current waveform is observed to be 22% lower than that of the [15] current. Additionally, the proposed current exhibits a 2.7% less rms current compared with the current in [15].

Fig. 16 displays the experimentally obtained frequency spectra of the stator core acceleration from the three accelerometers. Both the method in [15] and the proposed method exhibited notable reductions in the dominant acceleration peaks. For instance, accelerometers 1, 2, and 3 exhibit reductions of the ninth component by 12, 14, and 26 dB, respectively, under the proposed current. The highest acceleration peaks are concentrated in the region between the 54th and the 72nd frequency orders, corresponding to 5400 and 7200 Hz. This frequency range contains the mode-0 resonance frequency, hence the high acceleration peaks. The three accelerometers show reductions of the 63rd component, the highest component, by 17, 16, and 17 dB, respectively.

Fig. 17 shows the experimental SPL spectra. The most dominant SPL peaks were significantly mitigated. The 63rd
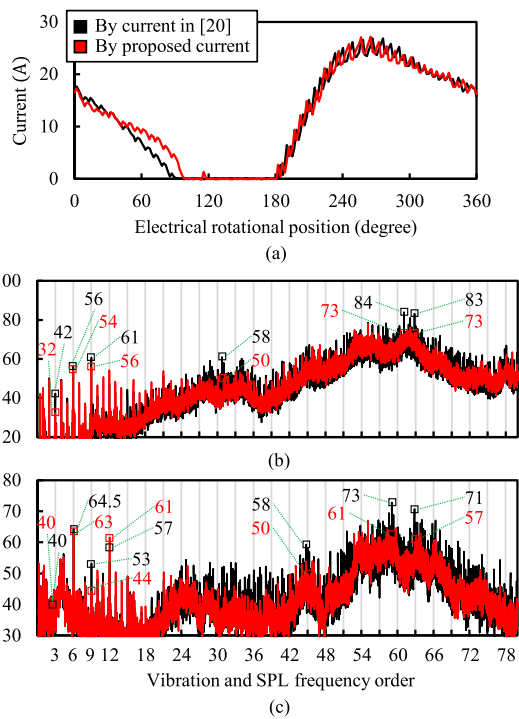
FIGURE 17. Experimental comparison of sound pressure level spectra between the conventional square method, radial-force shaping method in [15], and the proposed method.

and 66th components were reduced by 19 dB (98.7% reduction) and 23 dB (99.5% reduction), respectively. Other dominant peaks such as the sixth and 21st were remarkably reduced by the method in [15] and the proposed method. It is noteworthy that both methods are radial-force sum flattening methods, thus mainly targeting the multiples of the third component, which is responsible for exciting mode 0. It is observed from Figs. 16 and 17 both methods significantly reduced the multiples of the third component. Moreover, some of the nonmultiples of the third component were also reduced unintentionally.

B. PROPOSED METHOD COMPARISON WITH THE UNREFINED ANALYTICALLY-DERIVED METHOD

To verify the advantage of the proposed refinement method over that in [20], an experimental comparison is carried out in this subsection.

Fig. 18(a) shows the experimental comparison between the proposed refined current and the original analytically-derived current in [20] at 6.8 Nm. In Fig. 18(b) and (c), it is observed that the proposed method succeeded in significantly reducing the multiples of the third component in vibration and SPL. The majority of the multiples of the third are no longer among the dominant remaining peaks. In comparison with the original unrefined current in [20], the refined current resulted in even lower vibration and SPL, indicating the effectiveness of the refinement. Remarkably, the acceleration peaks at the third, sixth, and ninth harmonic orders are lower by 10 dB (90%), 2 dB (36.9%), and 5 dB (68.4%), respectively. Moreover, the acceleration peaks in the mode-0 resonance frequency region were reduced by 11 dB (92.1% reduction) and 10 dB (90% reduction), while the corresponding SPL peaks were reduced by 12 dB (93.7% reduction) and 14 dB (96% reduction), respectively. The calculated overall acceleration and sound pressure levels were 102.9 and 92.7 dB, respectively, for the method in [20], compared with 100.8 and 90.1 dB for the proposed method. From these experimental results obtained under a moderate saturation region, it can be concluded that the proposed refinement results in more reduction in the vibration and SPL than that resulting from the method in [20]. This advantage will be more significant in highly-saturated regions.

FIGURE 18. Experimental comparison between the analytically-derived current method from [20] and the proposed method (a) A-phase current waveforms, (b) acceleration spectra, and (c) sound pressure level spectra.
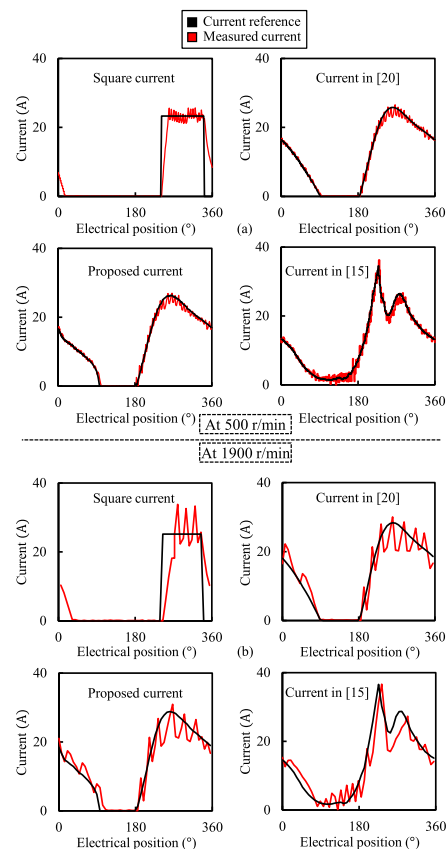
FIGURE 19. A-phase reference and measured currents at 6.8 Nm of the square, proposed, [20], and [15] methods at (a) 500 r/min and (b) 1900 r/min.
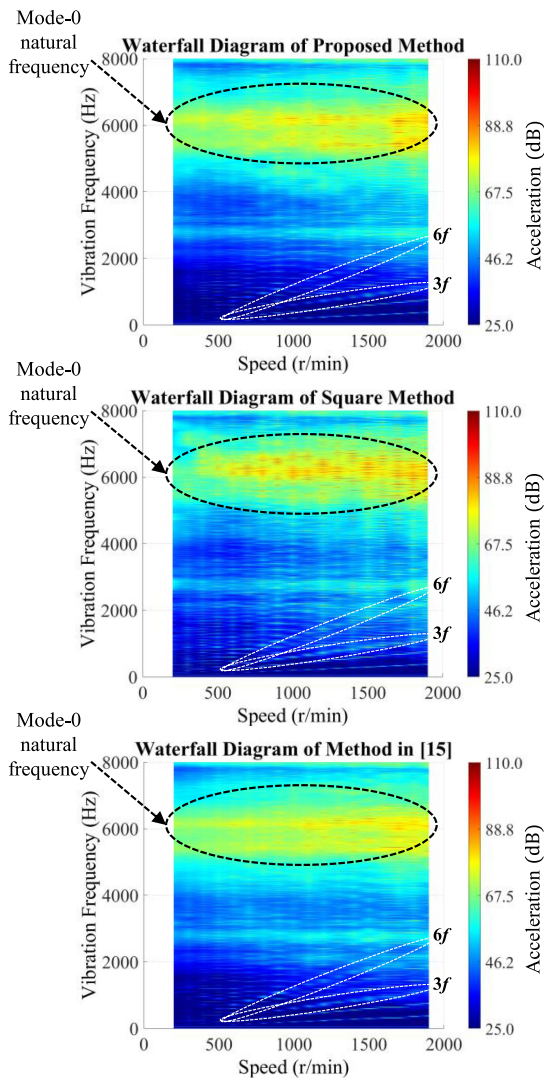
FIGURE 20. Experimental waterfall diagrams from accelerometer 1 for the proposed, square, and [15] methods at 6.8 Nm.

C. IMPACT OF SWITCHING FREQUENCY AND SRM SPEED ON THE PROPOSED METHOD

This subsection presents the experimental investigation of the impact of speed on the performance of the proposed method at the high torque value of 6.8 Nm, across the speed range of 200–1900 r/min.

It is noteworthy that at higher speeds, the switching frequency of the inverter imposes some limitations. As a result, the hysteresis current controller may not achieve a narrow hysteresis band at high speeds, leading to increased current ripple and distortions in the desired current waveform. The switching frequency of the SRM inverter adopted in this study is 20 kHz.

Fig. 19 illustrates the reference and measured currents at the high torque of 6.8 Nm for the square, proposed [20], and [15] methods at (a) 500 r/min and (b) 1900 r/min. It can be observed that at the lower speed of 500 r/min, all

the measured currents follow the references excellently. However, at the higher speed of 1900 r/min, distortions appear in the current waveforms. The proposed [20] and [15] currents exhibit ripples and deviations from their references at 1900 r/min. These current deviations can affect the reduction of the higher-order components of the radial force and vibration. To address this issue, employing Silicon-Carbide inverters, which can provide higher switching frequencies up to 100 kHz, is a recommended approach. It should be noted that the square currents in Fig. 19 are not ideal square currents as they return to zero after the aligned position of 360°.

Fig. 20 depicts the experimental waterfall diagrams captured from the stator accelerometer 1. It includes three diagrams representing the proposed method, the conventional square method, and the method in [15]. These diagrams are based on a torque setting of 6.8 Nm, while the speed of the SRM varies from 200 to 1900 r/min.

From the experimental waterfall diagrams in Fig. 20, it is evident that both the proposed method and the method in [15] achieved a reduction in the multiples of the third component compared with the square current method, with this reduction observed across the entire speed range. Additionally, the vibration in the mode-0 natural frequency spectrum, ranging from 5.5 to 6.5 kHz, was effectively reduced throughout the studied speed range. When comparing the proposed method to that in [15], the latter demonstrates slightly better performance in vibration reduction around the mode-0 natural frequency, but exhibits higher vibration in the low-frequency region.

V. CONCLUSION

This article introduces a refinement approach to the analytically-derived current waveform for vibration and acoustic noise reduction in SRMs. While the previously proposed analytically-derived current waveform in [20] effectively addressed acoustic noise in the low-torque region, its performance was limited in higher torque scenarios. The proposed refinement method overcomes this limitation, extending the applicability of the analytical derivation to include the high-torque region. Importantly, the refinement method achieves this without the need for numerical sweeping, maintaining the advantage provided by the analytical derivation approach. At 6.8 Nm, the proposed method achieved reductions of 19 and 23 dB of the highest two SPL peaks compared with the conventional square current. The highest two SPL peaks were also reduced by 12 and 14 dB compared with the method in [20]. As for the vibration highest two peaks, they were reduced by 17 and 26 dB when comparing the proposed method with the square current, and by 10 and 11 dB when comparing the proposed method with the method in [20].

Furthermore, the proposed refinement method is compared with another radial-force shaping method from the literature designed for the high-torque region. Both methods successfully flatten the radial-force sum in this region, indicated by the reduction of the highest vibration peak by 17 dB when comparing both methods to the square current, but the

proposed refinement method achieves this with notable advantages. Specifically, it demonstrates a 22% reduction in peak current and a 2.7% reduction in rms current compared with the method from the literature. This reduction in peak current alleviates the need for higher-rated inverters, providing additional cost savings. The effectiveness of the proposed method is validated across the speed range of 200–1900 r/min, where it was verified that the multiples of the third component were effectively reduced throughout the speed range. The vibration at the mode-0 natural frequency spectrum was significantly reduced as well.

APPENDIX I
SRM RADIAL AND TANGENTIAL CHARACTERISTICS IN THE MAGNETICALLY-LINEAR REGION

Specification	Unit	Using $K_r(\theta)$, $K_t(\theta)$ at 15 A dc current
K_{r0}	N/A^2	0.5912
K_{r1}	N/A^2	0.7538
K_{r2}	N/A^2	0.1308
K_{t1}	N/A^2	0.2829
K_{t2}	N/A^2	0.087
K_{t4}	N/A^2	0.061

APPENDIX II
THIRD-COMPONENT TERMS OF RADIAL-FORCE SUM

Term Index $F_{Sn}(3\theta)$	Term notation
$F_{S1}(3\theta)$	$\frac{3}{4}I_1^2 K_{r1}\cos(3\theta + 2\phi_1 + 180^o)$
$F_{S2}(3\theta)$	$3I_1 I_2 K_{r0}\cos(3\theta + \phi_1 + \phi_2 + 180^o)$
$F_{S3}(3\theta)$	$3I_0 I_1 K_{r2}\cos(3\theta + \phi_1 - 90^o)$
$F_{S4}(3\theta)$	$3I_0 I_2 K_{r1}\cos(3\theta + \phi_2 - 90^o)$
$F_{S5}(3\theta)$	$\frac{3}{2}I_1 I_2 K_{r2}\cos(3\theta - \phi_1 + \phi_2)$
$F_{S6}(3\theta)$	$\frac{3}{4}I_2^2 K_{r1}\cos(3\theta + 2\phi_2 + 180^o)$
$F_{S7}(3\theta)$	$6I_0 I_3 K_{r0}\cos(3\theta + \phi_3 - 90^o)$
$F_{S8}(3\theta)$	$\frac{3}{2}I_1 I_3 K_{r1}\cos(3\theta - \phi_1 + \phi_3)$
$F_{S9}(3\theta)$	$\frac{3}{2}I_1 I_3 K_{r1}\cos(3\theta + \phi_1 + \phi_3 + 180^o)$
$F_{S10}(3\theta)$	$\frac{3}{2}I_2 I_3 K_{r2}\cos(3\theta - \phi_2 + \phi_3)$
$F_{S11}(3\theta)$	$\frac{3}{2}I_2 I_3 K_{r2}\cos(3\theta + \phi_2 + \phi_3 + 180^o)$

$$F_{r_{Sum}}(3\theta) = \sum_{n=1}^{11} F_{Sn}(3\theta)$$

ACKNOWLEDGMENT

REFERENCES

[1] S. Das, O. Gundogmus, Y. Sozer, J. Kutz, J. Tylenda, and R. L. Wright, "Wide speed range noise and vibration mitigation in switched reluctance machines with stator pole bridges," *IEEE Trans. Power Electron.*, vol. 36, no. 8, pp. 9300–9311, Aug. 2021.

[2] A. Sohrabzadeh, H. Torkaman, and E. Afjei, "Torque ripple reduction and radial force mitigation in the switched reluctance motor using a novel rotor configuration," in *Proc. IEEE 14th Power Electron., Drive Syst., Technol. Conf.*, 2023, pp. 1–4.

[3] A. Sohrabzadeh, H. Torkaman, and A. Yousefi Javid, "Improvement undesirable characteristics of the switched reluctance motor with triangular rotor structure," *IEEE Trans. Energy Convers.*, vol. 38, no. 3, pp. 2118–2125, Sep. 2023.

[4] S. E. M. Mohammadi, P. Chen, M. Moallem, B. Fahimi, and M. Kiani, "An alternate rotor geometry for switched reluctance machine with reduced torque ripple," *IEEE Trans. Energy Convers.*, vol. 38, no. 2, pp. 939–947, Jun. 2023.

[5] K. Kiyota, T. Kakishima, A. Chiba, and M. A. Rahman, "Cylindrical rotor design for acoustic noise and windage loss reduction in switched reluctance motor for HEV applications," *IEEE Trans. Ind. Appl.*, vol. 52, no. 1, pp. 154–162, Jan./Feb. 2016.

[6] Y. Yasa, Y. Sozer, and M. Garip, "Acoustic noise mitigation of switched reluctance machines with leaf springs," *IEEE Trans. Ind. Electron.*, vol. 70, no. 2, pp. 1250–1260, Feb. 2023.

[7] O. Gundogmus et al., "Acoustic noise mitigation of switched reluctance machines with windows on stator and rotor poles," *IEEE Trans. Ind. Appl.*, vol. 56, no. 4, pp. 3719–3730, Jul./Aug. 2020.

[8] O. Gundogmus et al., "Acoustic noise mitigation in high pole count switched reluctance machines utilizing skewing method on stator and rotor poles," *IEEE Trans. Ind. Electron.*, vol. 69, no. 6, pp. 5581–5593, Jun. 2022.

[9] S. Shin, N. Kawagoe, T. Kosaka, and N. Matsui, "Study on commutation control method for reducing noise and vibration in SRM," *IEEE Trans. Ind. Appl.*, vol. 54, no. 5, pp. 4415–4424, Sep./Oct. 2018.

[10] J.-W. Ahn, S.-J. Park, and D.-H. Lee, "Hybrid excitation of SRM for reduction of vibration and acoustic noise," *IEEE Trans. Ind. Electron.*, vol. 51, no. 2, pp. 374–380, Apr. 2004.

[11] M. L. M. Kimpara et al., "Active cancellation of vibration in switched reluctance motor using mechanical impulse response method," *IEEE Trans. Energy Convers.*, vol. 34, no. 3, pp. 1358–1368, Sep. 2019.

[12] R. Pupadubsin, B. C. Mecrow, J. D. Widmer, and A. Steven, "Smooth voltage PWM for vibration and acoustic noise reduction in switched reluctance machines," *IEEE Trans. Energy Convers.*, vol. 36, no. 3, pp. 1578–1588, Sep. 2021.

[13] X. Guo, R. Zhong, M. Zhang, D. Ding, and W. Sun, "Resonance reduction by optimal switch angle selection in switched reluctance motor," *IEEE Trans. Ind. Electron.*, vol. 67, no. 3, pp. 1867–1877, Mar. 2020.

[14] A. D. Callegaro, B. Bilgin, and A. Emadi, "Radial force shaping for acoustic noise reduction in switched reluctance machines," *IEEE Trans. Power Electron.*, vol. 34, no. 10, pp. 9866–9878, Oct. 2019.

[15] F. S. El-Faouri, Y. Cai, A. Chiba, and Y. Fujii, "Acoustic noise reduction and radial-force sum flattening of switched reluctance motors by analytical force shaping," in *Proc. IEEE Energy Convers. Congr. Expo.*, 2023, pp. 4446–4450.

[16] M. Takiguchi, H. Sugimoto, N. Kurihara, and A. Chiba, "Acoustic noise and vibration reduction of SRM by elimination of third harmonic component in sum of radial forces," *IEEE Trans. Energy Convers.*, vol. 30, no. 3, pp. 883–891, Sep. 2015.

[17] J. Bayless, N. Kurihara, H. Sugimoto, and A. Chiba, "Acoustic noise reduction of switched reluctance motor with reduced RMS current and enhanced efficiency," *IEEE Trans. Energy Convers.*, vol. 31, no. 2, pp. 627–636, Jun. 2016.

[18] J. Furqani, C. A. Wiguna, A. Chiba, O. Gundogmus, Y. Sozer, and A. Purwadi, "Experimental verification of acoustic noise and radial force sum variation in switched reluctance motor," *IEEE Trans. Ind. Appl.*, vol. 57, no. 3, pp. 2481–2493, May/Jun. 2021.

[19] J. Furqani, M. Kawa, C. A. Wiguna, N. Kawata, K. Kiyota, and A. Chiba, "Current reference selection for acoustic noise reduction in two switched reluctance motors by flattening radial force sum," *IEEE Trans. Ind. Appl.*, vol. 55, no. 4, pp. 3617–3629, Jul./Aug. 2019.

[20] F. S. El-Faouri, Y. Cai, Y. Fujii, and A. Chiba, "Mathematical current derivation for acoustic noise reduction in switched reluctance motors," *IEEE Trans. Ind. Appl.*, vol. 60, no. 1, pp. 388–399, Jan./Feb. 2024.

[21] K. A. Kasper, J. O. Fiedler, D. Schmitz, and R. W. de Doncker, "Noise reduction control strategies for switched reluctance drives," in *Proc. IEEE Veh. Power Propulsion Conf.*, 2006, pp. 1–6.

[22] A. Hofmann, A. Al-Dajani, M. Bösing, and R. W. De Doncker, "Direct instantaneous force control: A method to eliminate mode-0-borne noise in switched reluctance machines," in *Proc. Int. Electric Mach. Drives Conf.*, 2013, pp. 1009–1016.

[23] C. Ma, L. Qu, R. Mitra, P. Pramod, and R. Islam, "Vibration and torque ripple reduction of switched reluctance motors through current profile optimization," in *Proc. IEEE Appl. Power Electron. Conf. Expo.*, 2016, pp. 3279–3285.

[24] O. Gundogmus, Y. Sozer, L. Vadamodala, J. Kutz, J. Tylenda, and R. L. Wright, "Current harmonics injection method for simultaneous torque and radial force ripple mitigation to reduce acoustic noise and vibration in SRMs," in *Proc. IEEE Energy Convers. Congr. Expo.*, 2019, pp. 7091–7097.

[25] A. Chiba et al., "Investigation of effective conditions of radial force sum flattening for acoustic noise reduction in switched reluctance motors," in *Proc. IEEE Energy Convers. Congr. Expo.*, 2022, pp. 1–7.

[26] B. Bilgin, J. W. Jiang, and A. Emadi, *Switched Reluctance Motor Drives: Fundamentals to Applications*. Boca Raton, FL, USA: CRC Press, 2018.

[27] A. Chiba et al., "Torque density and efficiency improvements of a switched reluctance motor without rare-earth material for hybrid vehicles," *IEEE Trans. Ind. Appl.*, vol. 47, no. 3, pp. 1240–1246, May/Jun. 2011.

[28] C. A. Wiguna et al., "Vibration and acoustic noise reduction in switched reluctance motor by selective radial force harmonics reduction," *IEEE Open J. Ind. Appl.*, vol. 4, pp. 23–34, Dec. 2022, doi: 10.1109/OJIA.2022.3229849.

[29] D. E. Cameron, J. H. Lang, and S. D. Umans, "The origin and reduction of acoustic noise in doubly salient variable-reluctance motors," *IEEE Trans. Ind. Appl.*, vol. 28, no. 6, pp. 1250–1255, Nov./Dec. 1992.

[30] G. R. Slemon, *Electronic Machines and Drives*. Reading, MA, USA: Addison-Wesley, 1992.

[31] Y. Cai, H. Sobue, C. A. Wiguna, A. Chiba, S. Yoshizaki, and K. Senda, "Radial electromagnetic force estimation using strain gauges in switched reluctance motors," *IEEE Trans. Ind. Appl.*, vol. 59, no. 2, pp. 1242–1252, Mar./Apr. 2023.

[32] N. Kawata and A. Chiba, "Design of switched reluctance generator for competitive energy efficiency in the latest hybrid electric vehicle," in *Proc. IEEE Energy Convers. Congr. Expo.*, 2018, pp. 6461–6467.

[33] H. Sobue et al., "Analysis and experimental comparison of acoustic noise of three switched reluctance motors made of conventional steel, high silicon steel, and amorphous iron," *IEEE Trans. Ind. Appl.*, vol. 57, no. 6, pp. 5907–5915, Nov./Dec. 2021.

[34] Y. Cai, F. S. El-Faouri, N. Saikawa, A. Chiba, and S. Yoshizaki, "Magnetostriction effect on vibration in switched reluctance motors," in *Proc. IEEE Energy Convers. Congr. Expo.*, 2023, pp. 4434–4441.

FARES S. EL-FAOURI (Graduate Student Member, IEEE) was born in Amman, Jordan, in 1993. He received the B.S. and M.S. degrees in electrical and electronic engineering from the Princess Sumaya University for Technology, Amman, Jordan, in 2015 and 2017, respectively. He is currently working toward the Ph.D. degree in electrical and electronic engineering with the Tokyo Institute of Technology, Tokyo, Japan.

His research interests include vibration and acoustic noise reduction in switched reluctance motors, and waveform shaping of current and radial force for the reduction of torque ripple, radial-force variation, and rms current.

YIFEI CAI (Graduate Student Member, IEEE) was born in Shanghai, China, in 1995. He received the B.S. and M.S. degrees in electrical and electronic engineering in 2018 and 2021, respectively, from the Tokyo Institute of Technology, Tokyo, Japan, where he is currently working toward the Ph.D. degree in electrical and electronic engineering.

He has been studying vibration and acoustic noise reduction in electric machines, electromagnetic force estimation in motors, magnetostriction of magnetic materials, magnetostriction effect in motor vibration, and acoustic noise. He is a Member of the Institute of Electrical Engineers of Japan and the Iron and Steel Institute of Japan.

AKIRA CHIBA (Fellow, IEEE) received the B.S., M.S., and Ph.D. degrees in electrical engineering from the Tokyo Institute of Technology, Tokyo, Japan, in 1983, 1985, and 1988, respectively.

In 1988, he joined the Tokyo University of Science as a Research Associate with the Department of Electrical Engineering, Faculty of Science and Technology. Since 2010, he has been a Professor with the School of Engineering, Tokyo Institute of Technology. He has been studying magnetically suspended bearingless ac motors, super high-speed motor drives, and rare-earth-free motors for hybrid and pure electric vehicles. He has so far authored or coauthored more than 1229 papers, including the first book on *Magnetic Bearings and Bearingless Drives* from Elsevier in 2005.

Dr. Chiba was the recipient of the First Prize Paper Award from the Electrical Machine Committee in the IEEE IAS in 2011 on a rare-earth-free motor, the second and third place Best Paper Awards in IEEE TRANSACTIONS ON ENERGY CONVERSION in 2016 and 2017, respectively, the IEEJ Prize Paper Awards in 1998, 2005, 2018, 2023, and 2020 IEEE Nikola Tesla Award, that is one of the IEEE Technical Field Awards. In 2023, he received the IEEE PES Cyril Veinott Electromechanical Energy Conversion Award. He served as the Secretary, Vice-Chair, Vice-Chair-Chair-Elect, Chair, and Past-Chair in the Motor Sub-Committee in the IEEE PES during 2007–2016. He has organized the Panel sessions and the combo sessions to activate the Motor Sub-Committee. He was the Technical Chair at IEEE IEMDC 2017 held in Miami, FL, USA, which was hosted by IEEE PES. He received the 2020 Distinguished Service Award from the Electric Machinery Committee in IEEE PES. He served as an Editor for IEEE TRANSACTIONS ON ENERGY CONVERSION in 2013–2024. He has served as the Secretary, Vice Chair, Chair, and Past Chair of the IEEE-IAS Electric Machine Committee during 2016–2023. He improved the relationship between PES and IAS electric machine-related committees. He was the ECCE Vice-Chair in 2016–2019. He was TCPRC and an Associate Editor for IEEE TRANSACTIONS ON INDUSTRY APPLICATIONS during 2020–2021 and 2011–2019, respectively. He served as one of the IEEE IAS Fellow Committee Executives from 2017 to 2020. He served as a Chair in IEEE-IAS Japan Chapter during 2010–2011. He was a Member, Chair, and Past-Chair of the IEEE Nikola Tesla Technical Field Award Committee during 2009–2014. He was a Member of the IEEE Power Medal Award Committee during 2021–2023. He was the Founding Chair of the Motor Technical Committee in the Japan Society of Automotive Society during 2012–2018. He was the Chair of the IEE-Japan Electric Machine Committee from 2020 to 2023. He has been serving as an Examiner in the Nagamori Award since 2015. He was the Department Head of the Electrical and Electronics Department during 2014–2016 and led the MOOC project of the introduction of Electrical and Electronics Engineering, released in 2017 through EDX. He has led active learning with the Internet Handbook application in undergraduate and graduate course lectures. He is currently the Head of the Electrical and Electronics Course in the Graduate School.